nature materials

ARTICLES

https://doi.org/10.1038/s41563-020-0775-8

Check for updates

Self-supported Pt–CoO networks combining high specific activity with high surface area for oxygen reduction

Gustav W. Sievers[1,2]✉, Anders W. Jensen[1], Jonathan Quinson[1], Alessandro Zana[1,3], Francesco Bizzotto[3], Mehtap Oezaslan[4,5], Alexandra Dworzak[4,5], Jacob J. K. Kirkensgaard[6,7], Thomas E. L. Smitshuysen[8], Shima Kadkhodazadeh[8], Mikkel Juelsholt[1], Kirsten M. Ø. Jensen[1], Kirsten Anklam[2], Hao Wan[1], Jan Schäfer[2], Klára Čépe[9], María Escudero-Escribano[1], Jan Rossmeisl[1], Antje Quade[2], Volker Brüser[2] and Matthias Arenz[1,3]✉

Several concepts for platinum-based catalysts for the oxygen reduction reaction (ORR) are presented that exceed the US Department of Energy targets for Pt-related ORR mass activity. Most concepts achieve their high ORR activity by increasing the Pt specific activity at the expense of a lower electrochemically active surface area (ECSA). In the potential region controlled by kinetics, such a lower ECSA is counterbalanced by the high specific activity. At higher overpotentials, however, which are often applied in real systems, a low ECSA leads to limitations in the reaction rate not by kinetics, but by mass transport. Here we report on self-supported platinum–cobalt oxide networks that combine a high specific activity with a high ECSA. The high ECSA is achieved by a platinum–cobalt oxide bone nanostructure that exhibits unprecedentedly high mass activity for self-supported ORR catalysts. This concept promises a stable fuel-cell operation at high temperature, high current density and low humidification.

Research and development of proton exchange membrane fuel cells (PEMFCs) have made substantial progress in recent years and reached industrial maturity in the serial production of fuel-cell cars by several automotive companies. This advancement is partly due to the rapid progress in engineering, but also due to more efficient fuel-cell catalysts[1–3]. At a research level, several catalysts have already shown catalytic activities capable of further reducing the amount of platinum (Pt) by a factor of five to ten[4], which is required for large-scale applications. Most catalysts reach high mass activities (MAs) by increasing the specific activity (SA) at the extent of a reduced electrochemical surface area (ECSA) as compared with those of standard platinum/carbon (Pt/C) catalysts[4–9].

The essential reaction in a PEMFC is the oxygen reduction reaction (ORR) to water:

$$O_2 + 4H^+ + 4e^- \rightarrow 2H_2O \quad (1)$$

As the oxygen reduction is kinetically inhibited, an overpotential is needed to start the reaction. At a relatively low overpotential, at which performance testing typically takes place, the reaction rate is limited by one of the charge-transfer reactions, that is, for Pt the reduction of the intermediates O*, OH* and OOH* (ref. [10]):

$$OH^* + H^+ + e^- \rightarrow H_2O \quad (2)$$

$$O^* + 2H^+ + 2e^- \rightarrow H_2O \quad (3)$$

$$OOH^* + 3H^+ + 3e^- \rightarrow 2H_2O \quad (4)$$

The binding energies of the individual reaction intermediates are connected via the scaling relation[10] and the discussion is usually based on a single reaction intermediate. If the hydroxyl binding energy is too small, the reaction is limited by the OH* reduction; if it is too large, the reaction is limited by the OOH* formation. As a consequence, the ORR activity displays a volcano-type dependence on the hydroxyl intermediate binding energy (Supplementary Fig. 1). To optimize the intermediate binding energies, the electronic structure of Pt has to be slightly changed. The principle areas in which to achieve this are strain and ligand effects[11,12], which are discussed later in more detail.

Automotive fuel-cell systems, however, operate at high current densities and thus relatively large overpotentials. As the overpotential increases, the nature of the rate-determining step changes and mass transfer becomes crucial for the performance[13–15]. As a consequence, at low overpotentials, and thus low current densities, the reduced ECSA of most catalyst concepts does not impact their performance[15]. However, at higher overpotentials, for example, 0.5 V, which is often reached under fuel-cell operation, the charge-transfer

[1]Department of Chemistry, University of Copenhagen, Copenhagen, Denmark. [2]Leibniz Institute for Plasma Science and Technology, Greifswald, Germany. [3]Department of Chemistry and Biochemistry, University of Bern, Bern, Switzerland. [4]Department of Chemistry, School of Mathematics and Science, Carl von Ossietzky University of Oldenburg, Oldenburg, Germany. [5]Technical Electrocatalysis Laboratory, Institute of Technical Chemistry, Technische Universität Braunschweig, Braunschweig, Germany. [6]Niels Bohr Institute, University of Copenhagen, Copenhagen, Denmark. [7]Department of Food Science, University of Copenhagen, Frederiksberg, Denmark. [8]Technical University of Denmark, Lyngby, Denmark. [9]Regional Centre of Advanced Technologies and Materials, Olomouc, Czech Republic. ✉e-mail: sievers@inp-greifswald.de; matthias.arenz@dcb.unibe.ch

steps are fast on an active catalyst[10] and mass transfer, especially oxygen resistance, becomes increasingly rate limiting[15]. Thus, the power density depends on the ECSA per mass and is key to achieve improved SAs and high ECSAs to realize a high performance in an automotive PEMFC application. As outlined in a recent work by Kongkanand et al.[15], a sole focus on optimizing the SA at low overpotentials disregards oxygen mass transport resistance occurring at higher overpotentials. Additionally, it was found that ionomer-free catalysts, such as nanostructured thin film (NSTF) catalysts have the lowest oxygen resistance[15]. For the goal to achieve high current densities $>1.5\,A\,cm^{-2}$ in fuel-cell operation, a high dispersion of the catalyst combined with a high specific activity is therefore crucial[15].

Here we present a concept for a self-supported catalyst capable of combining a high SA with an unprecedentedly high ECSA. The catalyst is inspired by developments for carbon-free ORR catalysts, such as NSTF catalysts introduced by 3M[8]. Such catalysts utilize the high SA of bulk Pt (ref. [8]), but perhaps equally important and technologically relevant, they circumvent the inherent carbon-corrosion problems of standard carbon-supported catalysts[8]. In addition, it was recently demonstrated that, in carbon-supported catalysts, it is not only oxygen diffusion that can be rate limiting, as so can proton transport[16]. Using new catalyst-layer engineering methods, oxygen-related mass transport resistances can be, to some extent, overcome[17,18]. A disruptive change of the catalyst layer concept towards self-supported catalyst layers would allow new operation regimes for PEMFCs with regard to temperature and humidification. The presented catalyst layer consists of a nanoporous (NP) Pt–cobalt oxide (Pt–CoO) network, which is achieved by alternating magnetron sputtering of Co and Pt layers and subsequent acid leaching of the non-noble CoO component (see Methods and Supplementary Information for more details). This method was recently applied to the synthesis of highly active self-supported iridium-based catalysts for oxygen evolution[19] and nanostructured Pt–Cu for ORR[20]; the latter presented a low ECSA as compared with that in this work. Compared with complex wet-chemical approaches, the magnetron sputtering technique can easily be scaled up and allows the use of different substrates, such as glassy carbon, but also gas diffusion layers, transfer foils or even membranes. The metal network is self-supported, that is, it does not require any carbon support material, and is directly prepared onto such substrates. In the presented work, we used glassy carbon disk electrodes and gas diffusion layers as substrates. In Fig. 1, scanning transmission electron microscopy (STEM) and scanning electron microscopy (SEM) micrographs are shown to visualize the porous structure. In addition, see the tomographic three-dimensional (3D) video (Supplementary Videos 1–3) and further corresponding information in Supplementary Figs. 2–6.

To investigate and optimize the NP Pt–CoO network, various catalysts with different Pt:Co starting compositions as well as heat-treatment steps were prepared, as summarized in Table 1. It was demonstrated that, after acid leaching (Methods), the catalyst could still contain up to 28.4 at% Co, as indicated by energy-dispersive X-ray spectroscopy (EDX) (Supplementary Fig. 7). However, X-ray photoelectron spectroscopy (XPS) revealed that, in all cases, the near-surface concentration of Co was very low (Table 1). A similar conclusion is suggested by high-angle annular dark-field (HAADF) STEM micrographs (Fig. 1), which show the elemental distribution at a nanometre scale. The presence of CoO under electrochemical conditions was confirmed by in situ X-ray absorption spectroscopy (XAS) (see below and Supplementary Information), whereas small-angle X-ray scattering (SAXS) indicated that a nanoporous structure was formed with a bone size of about 3–5 nm (Supplementary Fig. 6). This result is also in agreement with the transmission electron microscopy (TEM) analysis (Supplementary Fig. 3). Finally, it was found that a heating step in the synthesis led to a shift in the Pt 4*f* binding energy in the XPS spectra towards higher energies (Supplementary Fig. 8).

Testing the electrochemical performance of the catalysts in a rotating disk electrode (RDE) half-cell configuration revealed remarkable ORR activity (Fig. 2 and Table 1). At $0.9\,V_{RHE}$ (RHE, reversible hydrogen electrode), specific ORR current densities between 3.8 and $5.5\,mA\,cm^{-2}{}_{Pt}$ were observed. This correlates with an increase by a factor of ~8 as compared with a state-of-the-art supported Pt/C catalyst (TEC10E50E from Tanaka TKK) and a factor of ~2–3 compared with polycrystalline bulk Pt, which regularly serves as benchmark for the ORR[21]. Such ORR SAs are typical for highly active bulk Pt–alloy catalysts, such as Pt_3Co alloys. For instance, Stamenkovic et al. reported a ORR SA of around $4.5\,mA\,cm^{-2}{}_{Pt}$ at $0.9\,V_{RHE}$ for a polycrystalline Pt_3Co bulk alloy[3]. The high specific ORR performance can be related to an optimization of the binding energy of the catalyst surface with the reaction intermediates O, OH and OOH, which function as descriptors in the optimization of Pt-based ORR catalysts[22]. Alloying Pt with a second, less noble element, tunes the electronic structure of Pt and improves its ORR performance[23]. Furthermore, recently it was shown that surface distortion also has a positive effect on the ORR activity[2]. As mentioned above, the XPS results indicate that, in particular, heat treatment of the NP Pt–CoO networks leads to such a change of the electronic properties of Pt.

Stability measurements were performed at 80 °C with the accelerated stress (AST) protocols proposed by the Fuel Cell Commercialization Conference of Japan[24], which are described in detail in the Supplementary Information. A commercial Pt/C catalyst (TEC10E50E, 2–3 nm) was used as the benchmark. Applying an AST that simulated load cycles ($0.6–1\,V_{RHE}$; AST 1), a similar ~45% loss in the ECSA was found for the NP Pt–CoO networks as for the commercial Pt/C catalyst after 3,600 cycles. Nevertheless, the observed trend in ECSA loss during the AST treatment was different. Although under the applied conditions for the Pt/C catalyst a continuous 'exponential decrease' in ECSA was observed, the main ECSA loss of the NP Pt–CoO networks occurred in the first 600 AST cycles (Supplementary Fig. 13). Thereafter, the decrease in ECSA became slower. The degraded NP Pt–CoO networks were investigated by TEM and it was found that the degradation is related to an increase in the bone size of the networks, which most probably originates from the dissolution of Pt followed by redeposition on the bones as well as by dealloying (Supplementary Fig. 14). Such an effect is in good agreement with previous reports stating that an AST treatment that simulates load cycles mainly induces Pt dissolution and electrochemical Ostwald ripening[25]. Note that the TEM micrographs indicated no sign of changes in the structural morphology of the NP networks. On applying an AST treatment to simulate start–stop cycles ($1–1.5\,V_{RHE}$; AST 2), the advantage of the NP Pt–CoO networks over conventional catalyst concepts became evident, in particular the absence of a carbon support. Although, under the applied conditions, the Pt/C benchmark degraded very rapidly, 53% of the ECSA was lost after 800 cycles, and the self-supported Pt–CoO network catalyst was substantially more stable and lost only 15% of its surface area (Supplementary Figs. 15 and 16). Furthermore, the decrease in specific ORR activity was relatively moderate; after AST 2, the SA was still $3.6\,mA\,cm^{-2}{}_{Pt}$ as compared with a SA of $2.4\,mA\,cm^{-2}{}_{Pt}$ after AST 1 (Supplementary Fig. 17).

In comparing the electrocatalytic MA with previous efforts to optimize ORR catalysts, it is essential to note that with the catalysts developed in this work, the high SA of the NP Pt–CoO network is not achieved at the expense of a reduced ECSA (Fig. 2). Typically, going from bulk surfaces to nanoparticle-based catalysts, the specific ORR activity decreases as the particle size decreases[26]. In contrast, for the NP Pt–CoO networks, the achieved surface area is comparable with that of highly dispersed carbon-supported Pt nanoparticles, that is, $>100\,m^2\,g^{-1}{}_{Pt}$. Therefore, an initial loss of active surface area during 'load cycle treatments' is difficult to avoid.

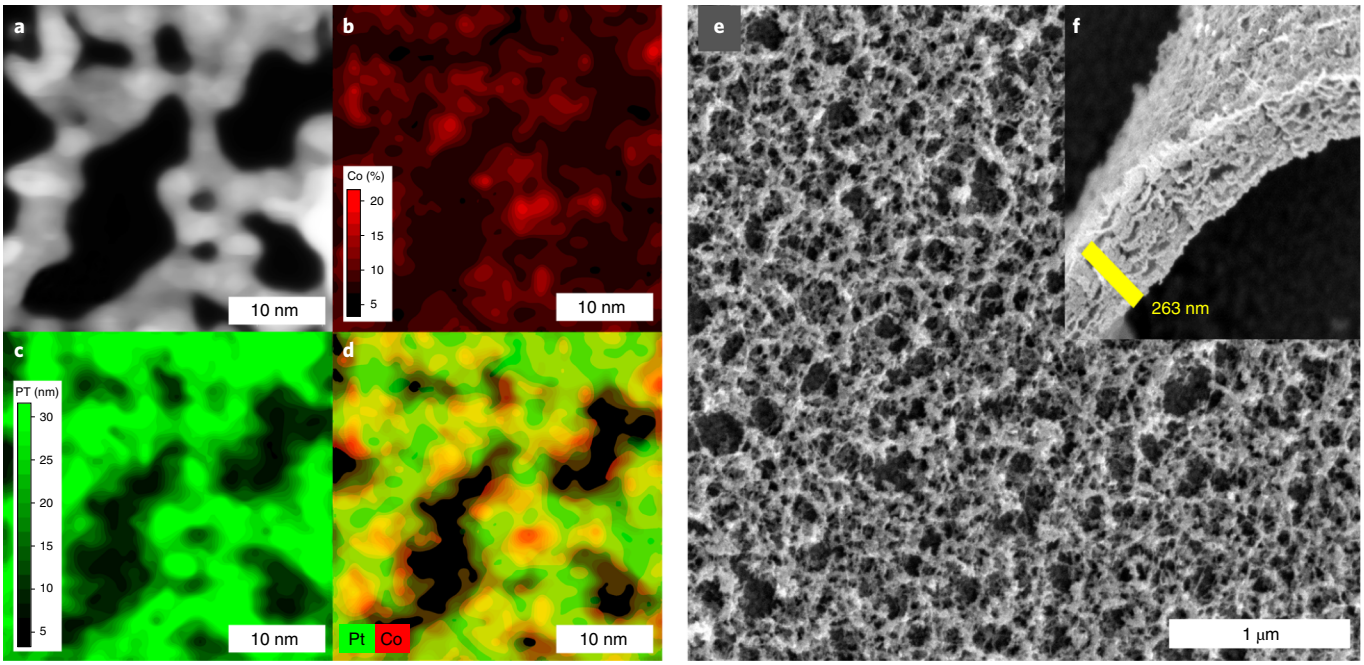

Fig. 1 | HAADF STEM and SEM images of self-supported nanoporous Pt–CoO networks. a–d, HAADF STEM images (**a**) with the elemental distributions of Pt–CoO measured by EDX for Co (red) (**b**), Pt (green) (**c**) and a combined elemental distribution map of Pt and Co (**d**). **e**,**f**, SEM top view (**e**) and side view (**f**).

Table 1 | Physical, chemical and electrochemical properties of differently prepared nanoporous Pt–CoO networks

	Pt–CoO 1	Pt–CoO 2	Pt–CoO 3	Pt–CoO heat 1	Pt–CoO heat 2
As-prepared Co:Pt weight ratio[a]	6.0	9.1	14.3	14.3	14.3
Co content[a] after leaching (at% Pt and Co)	17.5	28.4	10.4	21.2	26.5
Co content[b] after leaching (at% Pt and Co]	10.9	7.4	17.2	6.4	3.5
Peak position[b] after leaching, Pt(0) 4*f* (eV)	71.17	71.10	71.19	71.29	71.51
Bone size[c] (nm)	3.77	5.16	4.43	4.55	4.24
SA at 0.9 V_{RHE} ($mA\,cm^{-2}{}_{Pt}$)	4.57 ± 0.67	4.52 ± 0.30	3.77 ± 0.25	4.59 ± 0.17	5.38 ± 0.21
SA at 0.95 V_{RHE} ($mA\,cm^{-2}{}_{Pt}$)	0.52 ± 0.09	0.51 ± 0.02	0.49 ± 0.06	0.59 ± 0.02	0.62 ± 0.01
ECSA CO stripping ($m^2\,g^{-1}{}_{Pt}$)	101 ± 6	115 ± 4	152 ± 10	147 ± 6	156 ± 4
ECSA H-UPD ($m^2\,g^{-1}{}_{Pt}$)	85 ± 10	111 ± 28	147 ± 28	134 ± 25	156 ± 27
MA at 0.9 V_{RHE} ($A\,mg^{-1}{}_{Pt}$)	4.60 ± 0.96	5.19 ± 0.52	5.74 ± 0.76	6.75 ± 0.51	8.37 ± 0.55

[a]EDX. [b]XPS. [c]SAXS. Electrochemical activity as measured in the RDE (Supplementary Figs. 9–12). H-UPD, hydrogen underpotential deposition. Pt-CoO 1, Pt-CoO 2 and Pt-CoO 3 were prepared with different Co:Pt weight ratios as indicated in the Table. Pt-CoO heat 1 and Pt-CoO heat 2 were prepared using the Co:Pt ratio of Pt-CoO 3 and were subjected to an additional heat treatment.

However, after degradation the catalyst also retained a superior activity compared to that of standard catalysts. The high surface area of the NP Pt–CoO networks can be correlated to their nanoporous nature and fine Pt–CoO 'bone' structure with chain diameters of approximately 4 nm, as measured by SAXS and TEM (Table 1 and Supplementary Figs. 2–5). The pore diameter was averaged at approximately 16 nm (Supplementary Figs. 2 and 4). An estimation based on TEM tomography indicated that the mean volume of the bone structure was 20.4% (Supplementary Fig. 5). This combination of a fine bone structure and relatively large pore volume allows a high oxygen transport and high electronic conductivity. Furthermore, the presence of a Nafion ionomer in the catalyst layer of such a fuel cell is expected to be less crucial as compared with that in standard Pt/C or Pt alloy/C catalysts, as the proton transport can be established via proton diffusion on the surface of the catalyst or via adsorbed water, as emphasized by Debe[27] for ionomer-free catalyst layers.

As self-supported NP Pt–CoO networks are a new concept for ORR catalysts, we extensively characterized them further by both ex situ and in situ XAS, ex situ pair distribution function (PDF) analysis and computational modelling with density functional theory (DFT). The aim was to gain further knowledge on the structure–activity relationship as well as to understand better the nature of the active phase.

Ex situ X-ray absorption near-edge spectroscopy (XANES) and extended X-ray absorption fine structure (EXAFS) spectroscopy of the leached NP Pt–CoO networks at the Pt L_3 edge and Co K edge (Fig. 3, Supplementary Figs. 18–20 and Supplementary Table 3) indicated that the Pt was partially oxidized, whereas the Co largely appeared as CoO (Supplementary Fig. 19). The atomic Pt–Pt distances of the network catalyst were substantially reduced to values between 2.709 Å and 2.739 Å as compared with those of a Pt foil or even Pt nanoparticles supported on carbon ranging between 2.756 Å and 2.763 Å, which indicates a mean Pt–Pt lattice strain

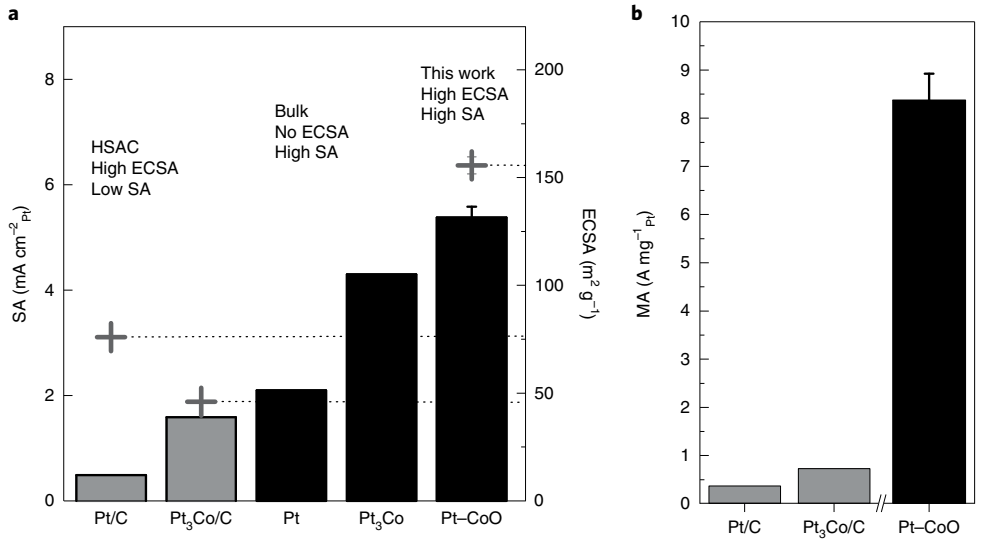

Fig. 2 | Comparison of ORR performance at 0.9 V_{RHE} for different standard and model catalysts with the best-performing NP Pt–CoO network. a, ORR SA (bars) and ECSA (plus signs). Grey bars, supported catalysts; black bars, self-supported/bulk catalysts. **b**, Pt-mass-related ORR activity calculated from **a**. The values for Pt/C (TEC10E50E 2–3 nm), Pt_3Co/C, Pt (polycrystalline, MA not available) and Pt_3Co (polycrystalline, MA not available) are taken from literature: Pt and Pt/C (ref. [35]), Pt_3Co (ref. [3]) and Pt_3Co/C (ref. [36]). HSAC, high surface area carbon.

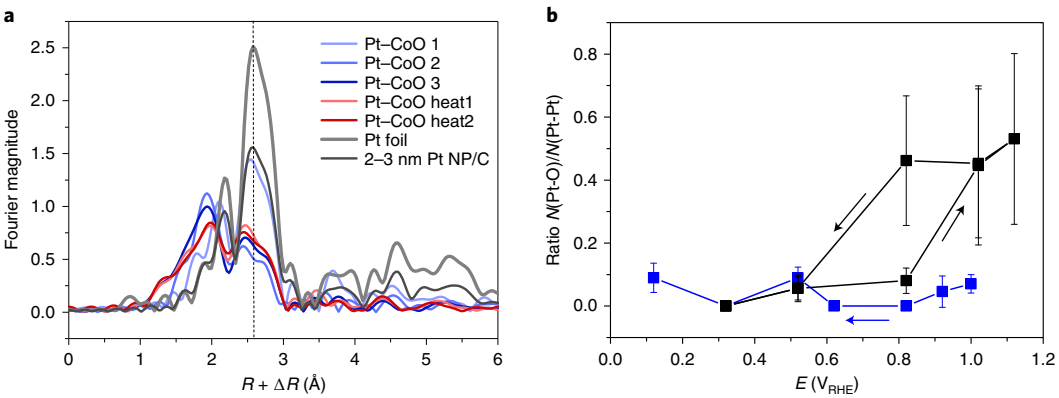

Fig. 3 | Ex situ and in situ XAS analysis. a, Fourier transform magnitudes of the k^2-weighted extended EXAFS data of the leached NP Pt–CoO networks (Pt L_3 edge). A pure Pt foil and Pt nanoparticles supported on carbon (Pt/C) with a mean particle size of 3–4 nm served as the references. The dashed line indicates the typical atomic Pt–Pt distance for 3-4 nm Pt/C and Pt foil. Note that the mean diameters of the Pt–CoO bones are similar to the mean diameter of the nanoparticles. The k range for the Fourier-transformed EXAFS spectra at the Pt L_3 edge was from 3 to 13 Å^{-1}. **b**, Potential-dependent N(Pt–O)/N(Pt–Pt) ratio measured in situ under electrochemical conditions. The coordination numbers of Pt–O and Pt–N were established by fitting the acquired EXAFS spectra. The arrows on the Pt–CoO (blue) and Pt/C 30 wt% (black) curves show the change in direction of the measured potentials. The error bars indicate the uncertainty provided from the fitting of the spectra using the IFEFFIT software package. The lines connecting the points serve as guide for the eye.

(Supplementary Table 3). Also note that no Pt–Co alloy was formed; the EXAFS spectra for the NP Pt–CoO networks reveal the absence of heterometallic Pt–Co pairs. That is, the alternated magnetron sputtering and dealloying largely led to monometallic Pt–CoO bone structures without alloy formation. PDF analysis of X-ray total scattering data (Fig. 4 and Supplementary Tables 4 and 5) showed that the leached NP Pt–CoO networks exhibit mainly an face-centred cubic (fcc) structure that corresponds to a strained Pt nanostructure with a smaller unit-cell parameter compared with that of bulk Pt, which confirms the EXAFS results. The structure is highly strained: although all the peaks in the PDF can be assigned to an fcc structure, the apparent unit-cell parameter changes when the structure modelling is done over different ranges of the PDF (Supplementary Tables 4 and 5). Such behaviour may be explained by the presence of Co or CoO in the structures or a curvature of the thin bones in the structure. Note that the lower X-ray scattering power of Co compared with that of Pt and the low concentration of Co makes it difficult to establish the structure of the Co-containing phases using the current X-ray total scattering data.

The presence of CoO in the leached NP Pt–CoO networks is in agreement with the formation of Pt–CoO structures in which Co is preferentially encapsulated in the core and Pt dominates at the surface. To investigate the effect of CoO on a thin Pt skin, we performed DFT calculations to model the strain effect in such structures (see Supplementary Figs. 21 and 22 and the discussion in the Supplementary Information). The calculations indicate that the induced compressive strain (–1.28%) weakens the adsorption of OH by 0.038 eV, which leads to an estimated reduction of around 38 mV in overpotential as compared with that in an unstrained Pt layer. The relative strain is in agreement with that of electronically

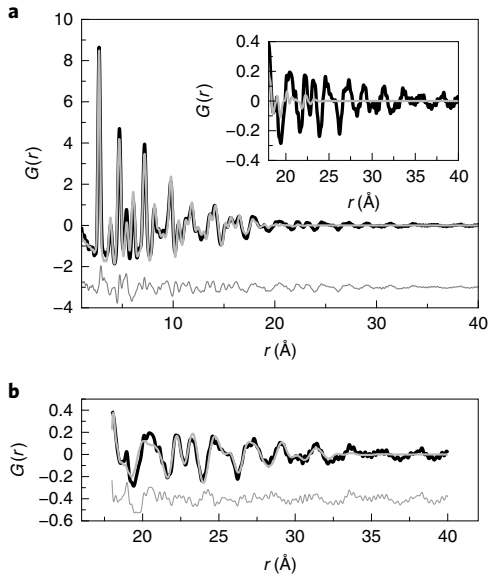

Fig. 4 | X-Ray total scattering. a, Fit of the fcc structure to the experimental PDF from a leached Pt–CoO sample. The fcc structure fits to the most intense peaks in the low *r* region. Inset: magnification of the fit in the *r* range from 18 to 40 Å, where the model fails to fit the experimental data. **b**, The high *r* data can be fitted by a fcc model, although with a smaller unit-cell parameter.

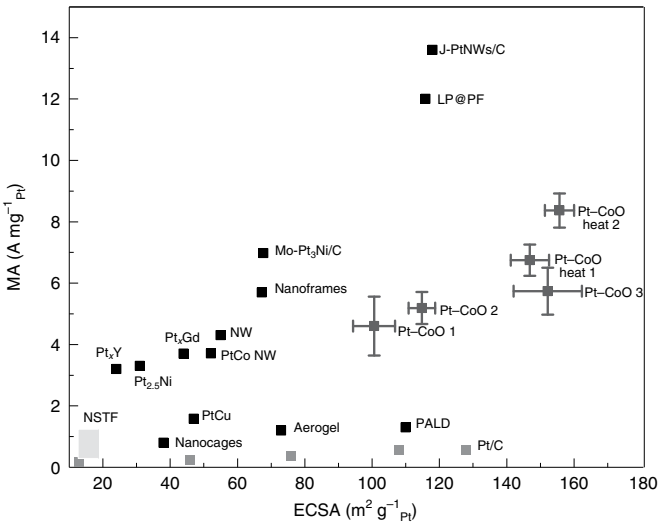

Fig. 5 | Comparison of ORR MAs. MAs at 0.9 V_{RHE} and ECSA for different supported and self-supported catalysts, which include the self-supported NP Pt-CoO networks in this work. The error bars indicate the respective standard deviation of the ECSA and MA in three samples. Supported: nanocages[5], nanoframes[4], $Pt_{2.5}Ni$ (ref. [6]), Pt_xGd (ref. [7]), NSTF[8], Pt/C (ref. [35]), J-PtNWs/C (ref. [32]), Pt_xY (ref. [28]), PtCo nanowire[37], Mo-Pt_3Ni/C (ref. [38]), ultralow concentration of Pt alloy supported over PGM-free materials (LF@PF)[39], nanoplate[40] and passivation-gas-incorporated atomic layer deposited Pt/C (PALD)[41]. Self-supported: PtCu (ref. [20]) and aerogel[42].

modified Pt electrocatalysts, as found for Pt_xY (ref. [28]) and dealloyed Pt–Cu (ref. [29]), and is known to increase the ORR activity[12]. The calculations are in line with in situ EXAFS measurements (Fig. 3 and Supplementary Information), which show that, indeed, in the NP Pt–CoO networks, the Pt–O coordination as a function of the applied potential is substantially lower than that of a Pt/C benchmark sample. As no contribution of the Co–Pt pairs was observed from the ex situ XAS data, we assume that the coordination number of the Pt is altered by the anodic potential applied during the ORR, with oxygen species adsorbed at the electrode surface.

In addition, small amounts of CoO might be present on the Pt surface as well. It is well-known that metallic Co dissolves under the given electrochemical conditions. However, recently a strong stabilization effect of thin transition-metal-oxide films of transition metals (for example, Co) on Pt was shown[30]. Owing to hybridized electronic orbitals[30], the stability region of such nano-oxide films is substantially extended as compared with that of their bulk metal oxide counterparts. Therefore, CoO formed on air exposure on porous nanolayers of Co/Pt might be stabilized by the adjacent Pt layer and so prevent its (complete) dissolution under electrochemical reaction conditions. In a different context, it was shown that $CoFePbO_x$ catalysts formed in situ exhibit high acid resistance due to a self-healing mechanism and can even serve as catalysts for the oxygen evolution reaction[31].

The combination of a high SA with a high ECSA leads to extremely high MAs for the ORR. As summarized in Fig. 5 and Table 1, the highest-achieved MA reached 8 A mg^{-1}_{Pt} at 0.9 V_{RHE}. This exceeds the performance of conventional, carbon-supported Pt–alloy catalysts by a factor of ~15 (Fig. 2). To the best of our knowledge, the MAs of the here presented self-supported NP Pt–CoO networks are far superior to those of previously reported carbon-free ORR catalysts. Similar or higher MAs were previously observed only for systems that require a carbon support, such as reported Pt–Ni nanoframes[4] or ultrafine jagged Pt nanowires (J-PtNWs/C)[32].

To conclude, the combination of a high ORR SA and high ECSA leads to high MA values of the self-supported NP Pt–CoO networks. The higher SA is assigned to a strained Pt surface caused by the CoO core. In addition, Co nano-oxide films might be present on the Pt bone structures, which further boosts the activity. As well as being a model catalyst, this new type of self-supported catalyst is an important step towards applications of PEMFCs because the key property of improved SAs and high ECSAs is not only important to obtain a high MA, but is also expected to be crucial to realize such a performance in a PEMFC application. Optimizing these kinds of catalyst layers for PEMFCs will require larger catalyst layers that enable extensive membrane electrode assembly testing, as has been done with carbon-supported catalysts for decades. For a more realistic benchmarking test, we also measured the Pt––CoO network catalyst in a gas diffusion electrode half-cell set-up[14,33] (Supplementary Fig. 23). As a promising result, it was confirmed that the activity of this catalyst is, indeed, superior to Pt/C at a low temperature and in dry conditions. However, under humidified conditions and a high temperature, such as 80 °C, the catalyst layer has to be further optimized to avoid flooding. Nevertheless, the target in the automotive industry is to develop PEMFCs operable above 100 °C to reduce problems in heat management, conditions at which flooding should not be a problem but carbon corrosion is expected to increase[34]. At such conditions, carbon-free self-supported catalyst concepts will be particularly interesting. This work presents a new approach to derive such electrocatalysts and demonstrates that highly active catalysts are achievable without support materials, which should inspire the development of the next generation of ORR catalysts. The presented technology is industrially scalable and can be applied on all planar surfaces, such as gas diffusion layers, transfer foils or membranes. Thus, it combines all the necessary ingredients to enable a further decrease in the Pt content of future PEMFC technologies for mobile applications.

Online content

Any methods, additional references, Nature Research reporting summaries, source data, extended data, supplementary information, acknowledgements, peer review information; details of author contributions and competing interests; and statements of

data and code availability are available at https://doi.org/10.1038/s41563-020-0775-8.

Received: 3 April 2020; Accepted: 15 July 2020;
Published online: 24 August 2020

References

1. Banham, D. W. H. & Ye, S. Current status and future development of catalyst materials and catalyst layers for PEMFCs: an industrial perspective. *ACS Energy Lett.* **2**, 629–638 (2017).
2. Chattot, R. et al. Surface distortion as a unifying concept and descriptor in oxygen reduction reaction electrocatalysis. *Nat. Mater.* **17**, 827–833 (2018).
3. Stamenkovic, V. R. et al. Trends in electrocatalysis on extended and nanoscale Pt–bimetallic alloy surfaces. *Nat. Mater.* **6**, 241–247 (2007).
4. Chen, C. et al. Highly crystalline multimetallic nanoframes with three-dimensional electrocatalytic surfaces. *Science.* **343**, 1339–1343 (2014).
5. Zhang, L. et al. Platinum-based nanocages with subnanometer-thick walls and well-defined, controllable facets. *Science* **349**, 412–416 (2015).
6. Choi, S.-I. et al. Synthesis and characterization of 9 nm Pt–Ni octahedra with a record high activity of 3.3 A/mg Pt for the oxygen reduction reaction. *Nano Lett.* **13**, 3420–3425 (2013).
7. Velázquez-Palenzuela, A. et al. The enhanced activity of mass-selected Pt_xGd nanoparticles for oxygen electroreduction. *J. Catal.* **328**, 297–307 (2015).
8. Debe, M. K. Electrocatalyst approaches and challenges for automotive fuel cells. *Nature* **486**, 43–51 (2012).
9. Liu, W. et al. Noble metal aerogels—synthesis, characterization, and application as electrocatalysts. *Acc. Chem. Res.* **48**, 154–162 (2015).
10. Stephens, I., Bondarenko, A., U, G., Rossmeisl, J. & Chorkendorff, I. Understanding the electrocatalysis of oxygen reduction on platinum and its alloys. *Energy* **5**, 6744–6762 (2012).
11. Escudero-Escribano, M., Jensen, K. D. & Jensen, A. W. Recent advances in bimetallic electrocatalysts for oxygen reduction: design principles, structure–function relations and active phase elucidation. *Curr. Opin. Electrochem.* **8**, 135–146 (2018).
12. Escudero-Escribano, M. et al. Tuning the activity of Pt alloy electrocatalysts by means of the lanthanide contraction. *Science* **352**, 73–76 (2016).
13. Zalitis, C. M., Kramer, D. & Kucernak, A. R. Electrocatalytic performance of fuel cell reactions at low catalyst loading and high mass transport. *Phys. Chem. Chem. Phys.* **15**, 4329–4340 (2013).
14. Inaba, M. et al. Benchmarking high surface area electrocatalysts in a gas diffusion electrode: measurement of oxygen reduction activities under realistic conditions. *Energy Environ. Sci.* **11**, 988–994 (2018).
15. Kongkanand, A. & Mathias, M. F. The Priority and Challenge of High-Power Performance of Low-Platinum Proton-Exchange Membrane Fuel Cells. *J. Phys. Chem. Lett.* **7**, 1127–1137 (2016).
16. Costentin, C., Di Giovanni, C., Giraud, M., Savéant, J. M. & Tard, C. Nanodiffusion in electrocatalytic films. *Nat. Mater.* **16**, 1016–1021 (2017).
17. Ott, S. et al. Ionomer distribution control in porous carbon-supported catalyst layers for high-power and low Pt-loaded proton exchange membrane fuel cells. *Nat. Mater.* https://doi.org/10.1038/s41563-019-0487-0 (2019).
18. Orfanidi, A., Rheinländer, P. J., Schulte, N. & Gasteiger, H. A. Ink solvent dependence of the ionomer distribution in the catalyst layer of a PEMFC. *J. Electrochem. Soc.* **165**, F1254–F1263 (2018).
19. Jensen, A. W. et al. Self-supported nanostructured iridium-based networks as highly active electrocatalysts for oxygen evolution in acidic media. *J. Mater. Chem. A* **8**, 1066–1071 (2020).
20. Sievers, G., Bowen, J. R., Brüser, V. & Arenz, M. Support-free nanostructured Pt–Cu electrocatalyst for the oxygen reduction reaction prepared by alternating magnetron sputtering. *J. Power Sources* **413**, 432–440 (2019).
21. Gasteiger, H. A., Kocha, S. S., Sompalli, B. & Wagner, F. T. Activity benchmarks and requirements for Pt, Pt–alloy, and non-Pt oxygen reduction catalysts for PEMFCs. *Appl. Catal. B* **56**, 9–35 (2005).
22. Nørskov, J. K. et al. Origin of the overpotential for oxygen reduction at a fuel-cell cathode. *J. Phys. Chem. B* **108**, 17886–17892 (2004).
23. Stamenkovic, V. et al. Changing the activity of electrocatalysts for oxygen reduction by tuning the surface electronic structure. *Angew. Chem. Int. Ed.* **45**, 2897–2901 (2006).
24. Zana, A., Speder, J., Reeler, N. E. A., Vosch, T. & Arenz, M. Investigating the corrosion of high surface area carbons during start/stop fuel cell conditions: a Raman study. *Electrochim. Acta* **114**, 455–461 (2013).
25. Zana, A. et al. Probing degradation by IL-TEM: the influence of stress test conditions on the degradation mechanism. *J. Electrochem. Soc.* **160**, F608–F615 (2013).
26. Wang, C. et al. Monodisperse Pt_3Co nanoparticles as a catalyst for the oxygen reduction reaction: size-dependent activity. *J. Phys. Chem. C* **113**, 19365–19368 (2009).
27. Debe, M. K. Tutorial on the fundamental characteristics and practical properties of nanostructured thin film (NSTF) catalysts. *J. Electrochem. Soc.* **160**, F522–F534 (2013).
28. Hernandez-Fernandez, P. et al. Mass-selected nanoparticles of Pt_xY as model catalysts for oxygen electroreduction. *Nat. Chem.* **6**, 732–738 (2014).
29. Strasser, P. et al. Lattice-strain control of the activity in dealloyed core–shell fuel cell catalysts. *Nat. Chem.* **2**, 454–460 (2010).
30. Zeng, Z., Chang, K. C., Kubal, J., Markovic, N. M. & Greeley, J. Stabilization of ultrathin (hydroxy)oxide films on transition metal substrates for electrochemical energy conversion. *Nat. Energy* **2**, 17070 (2017).
31. Chatti, M. et al. Intrinsically stable in situ generated electrocatalyst for long-term oxidation of acidic water at up to 80 °C. *Nat. Catal.* **2**, 457–465 (2019).
32. Li, M. et al. Ultrafine jagged platinum nanowires enable ultrahigh mass activity for the oxygen reduction reaction. *Science* **354**, 1414–1419 (2016).
33. Sievers, G., Jensen, A. W., Brüser, V., Arenz, M. & Escudero-Escribano, M. Sputtered platinum thin-films for oxygen reduction in gas diffusion electrodes: a model system for studies under realistic reaction conditions. *Surfaces* **2**, 336–348 (2019).
34. Suzuki, T. et al. Toward the Future Fuel Cell—Challenge for 2040. *ECS Trans.* **92**, 3–7 (2019).
35. Nesselberger, M. et al. The particle size effect on the oxygen reduction reaction activity of Pt catalysts: influence of electrolyte and relation to single crystal models. *J. Am. Chem. Soc.* **133**, 17428–17433 (2011).
36. Spanos, I., Kirkensgaard, J. J. K., Mortensen, K. & Arenz, M. Investigating the activity enhancement on Pt_xCo_{1-x} alloys induced by a combined strain and ligand effect. *J. Power Sources* **245**, 908–914 (2014).
37. Bu, L. et al. Surface engineering of hierarchical platinum–cobalt nanowires for efficient electrocatalysis. *Nat. Commun.* **7**, 11850 (2016).
38. Huang, X. et al. High-performance transition metal-doped Pt_3Ni octahedra for oxygen reduction reaction. *Science* **348**, 1230–1234 (2015).
39. Chong, L. et al. Ultralow-loading platinum–cobalt fuel cell catalysts derived from imidazolate frameworks. *Science* **1281**, 1276–1281 (2018).
40. Bu, L. et al. Biaxially strained PtPb/Pt core/shell nanoplate boosts oxygen reduction catalysis. *Science* **354**, 1410–1414 (2016).
41. Xu, S. et al. Extending the limits of Pt/C catalysts with passivation-gas-incorporated atomic layer deposition. *Nat. Catal.* **1**, 624–630 (2018)
42. Liu, W. et al. Bimetallic aerogels: high-performance electrocatalysts for the oxygen reduction reaction. *Angew. Chem. Int. Ed.* **52**, 9849–9852 (2013).

Methods

Sample preparation. Glassy carbon electrodes (3 and 5 mm in diameter; HTW) were polished and ultrasonicated in acetone, isopropanol, ethanol and ultrapure H_2O (Millipore 18.2 MΩ cm resistance and 5 ppb total organic carbon). The electrodes were thereafter transferred to a vacuum chamber and, for 3 min, plasma activated at a pressure of 20 Pa in an O_2 atmosphere and a radio-frequency power of 300 W. Samples were then transferred to the deposition chamber. To prepare the Pt–Co catalysts, the reactor chamber was evacuated to a base pressure of 5×10^{-3} Pa. An argon plasma was ignited in the chamber at a working pressure of 5 Pa. First, a 15 nm Ti (99.9%, Mateck GmbH) interlayer was deposited onto the glassy carbon by magnetron sputtering. For the Pt–Co film deposition, two magnetrons were equipped with planar targets of Co (99.9%, Mateck GmbH) and Pt (99.95%, Junker Edelmetalle). They were located at the superior part of the recipient. The radio-frequency generators (Advanced Energy) had a driving frequency of 13.56 MHz. The recipient (Neoplas GmbH) was configurated in such a way that the substrate holder turned automatically towards the respective magnetron with the sputtering being initiated when the sample was in position below the magnetron. To obtain the nanoporous metal film, Co and Pt sputtering were alternated with the respective loading deposition of Pt and Co. The alternating process was repeated 11 times so that the total Pt loading of the as-deposited electrode was 22 $\mu g_{Pt}\,cm^{-2}{}_{geo}$ (geo, geometric). We varied the deposition time of Co to obtain different Co:Pt compositions, respectively 6:1, 9:1 and 14:1 by weight. Directly after preparation, Pt–CoO heat 1 and Pt–CoO heat 2 metal films with a similar Co:Pt ratio as Pt-CoO 3 (14:1) were treated in the vacuum chamber at 573 K for 8 (heat 1) and 16 (heat 2) min. After deposition of the NP Pt–CoO networks, the glassy carbon electrode was inserted into a Teflon holder. Then, samples were electrochemically leached by inserting them under a potential control into the electrochemical cell and cycling them between 0.05 and 1.00 V_{RHE} with a scan rate of 50 mV s^{-1}, directly after immersion into a de-aerated 0.1 M $HClO_4$ electrolyte until a stable cyclic voltammogram was achieved. As a control, the Pt and Co contents of the metal films were determined by EDX before and after leaching. Each sample was prepared and tested at least three times.

Electrochemical investigations. The tips were mounted as working electrodes into the RDE and placed in a separate three-compartment electrochemical Teflon cell. The reference electrode was separated from the working electrode by a Nafion membrane[43]. All the measurements were performed at room temperature using a Nordic-EC potentiostat, a saturated calomel reference electrode and a carbon rod as the counter electrode. Prior to each experiment the potential was calibrated to the RHE. The solution resistance was electronically compensated by a positive feedback scheme. The potentials in this study are given with respect to the RHE. In all measurements, 0.1 M $HClO_4$ was used as the electrolyte. The electrolytes were made from MilliQ water (>18.2 MΩ cm, <5 ppb total organic carbon) and ultrapure 70% $HClO_4$ (Suprapur, Merck). SA was defined as the quotient of the kinetic activity as calculated by the Koutecky–Levich equation divided by ECSA determined by the CO stripping method. ECSA was defined as the surface area determined by CO stripping divided by the measured Pt mass with inductively coupled plasma mass spectrometry (ICP-MS) after leaching and ORR testing. The MA was defined as the SA multiplied by the ECSA. For the calculation of the ECSA, we used the loading, as measured by ICP-MS, after leaching, because more than half of the Pt was lost during leaching. For further information see the Supplementary Information.

SEM and TEM characterization. The SEM (JSM7500F, Jeol) was employed with a field-emission gun, a semi in-lens conical objective lens and a secondary electron in-lens detector for high-resolution and high-quality imaging of the structural features. The maximum specified resolution was 1.0 nm at 15 keV. Glassy carbon electrodes were directly positioned on the substrate holder without any preparative coating. The TEM (Jeol 2100) was operated at 200 kV. Samples were characterized by recording images with a minimum of three different magnifications in at least five different areas of the TEM grid. The size analysis was performed by measuring the size of the skeleton. The TEM grids were prepared as follows. The glassy carbon disc with the nanoporous catalyst layer was sonicated in ~200–500 µl of isopropanol for 5 min until the isopropanol turned slightly grey, which indicates the dispersion of the sample. This dispersion was then drop cast onto a holey carbon support film of Cu 300 mesh grids (Quantifoil). In addition, we deposited Pt–Co templates directly onto the TEM grids and leached them in 0.1 M perchloric acid prior to the TEM investigations. The size of the different structures in the TEM images was analysed using imageJ software by manually measuring the size of the different structures and classifying them into pore, bone and agglomerate.

Scanning transmission electron tomography. The electron tomography data were acquired in the HAADF STEM mode on a Thermo Fisher Titan (S)TEM instrument fitted with a field emission electron gun and operated at 300 kV. The electron probe size and convergence angle were ~1.5 Å and 17 mrad, respectively, and the HAADF collection angle was 50 mrad. Tilt series in the angular range −68° to +68° were acquired with 2° increment steps. The shift between the images in the tilt series and their rotation axis were corrected using the Thermo Fisher Inspect3D program. The SIRT algorithm was used to reconstruct the 3D structure from the aligned tilt series. The 3D visualization and volume rendering was performed in the program Aviso Lite 9.0.1.

HAADF STEM imaging. The samples were measured by a high-resolution TEM Titan G2 (FEI) with an Image corrector and an accelerating voltage of 80 kV. STEM images were taken with the HAADF detector Model 3000 (Fishione). The qualitative EDX mapping was obtained by a Super-X system with four silicon drift detectors (Bruker) in STEM mode at 80 kV (Titan G2, FEI). The collected data were evaluated by a Cliff–Lorimer model and averaged at a lateral map resolution of 1 nm.

EDX and XPS characterization. the Pt to Co ratios were analysed by EDX and XPS. EDX was performed with a SEM (JSM7500F, JEOL) using 10 keV and higher beam currents. XPS was carried out using an Axis Ultra (Kratos) for element analysis and determination of the electronic density of states. The spectra were recorded by means of monochromatic Al Kα excitation (1.486.6 eV) with a medium magnification (field of view 2) lens mode and by selecting the slot mode, which provides an analysis area of approximately 250 µm in diameter. A pass energy of 80 eV was used to estimate the chemical elemental composition; 10 eV was used for the high-energy resolution of the Pt 4*f* region to investigate the Pt chemical state.

ICP-MS measurements. The Pt loading of the catalysts was determined by using ICP-MS measurements. For this, the catalysts were digested in aqua regia freshly mixed with 30% HCl (Suprapur, Merck) and 65% HNO_3 (Suprapur, Merck) in a volumetric ratio of 3:1, respectively. This process was repeated once. Then the samples were dissolved in 5–10 ml Aqua Dest. The samples were thereafter diluted 1:10 for the ICP-MS analysis. The concentration of Pt in the diluted aqua regia solution was analysed by ICP-MS (NexION 300X, Perkin Elmer) through a Meinhard quartz nebulizer and a cyclonic spray chamber, operated at nebulizer gas flow rates of between 1.00 and 1.02 l min^{-1} (Ar, purity grade 5.0).

SAXS analysis. SAXS profiles were measured using the SAXSLab instrument at the Niels Bohr Institute. The instrument uses a Rigaku 40 W microfocused Cu source to produce X-rays with a wavelength of $\lambda = 1.54$ Å detected by a moveable Pilatus 300K pixel-detector allowing different q-ranges to be measured. Here the magnitude of the scattering vector is defined as $q = 4\pi\sin\theta/\lambda$ with θ being half the scattering angle. The q calibration of the instrument was done using silver behenate. The scattering data were analysed using the following expression:

$$I(q) = Aq^{-n} + B + \frac{C}{(1 + R^2q^2)^2}$$

where A and C are constants, n is the Porod exponent of the power law that describes surface scattering, B is a small constant term that accounts for the background scattering from the thin quartz plates that the samples are mounted on and, finally, the last term describes the scattering from the metal network with the main fit parameter, the network radius R. The term originates from pore structure analysis[44], but from Babinet's principle the scattering signal is the same whether the pore is empty or, as in this case, filled.

XAS analysis. XANES and EXAFS measurements were carried out at the B18 beamline, Diamond Light Source, and at the beamline SuperXAS X10DA, Swiss Light Source. The in situ XAS experiments were performed at the ROCK beamline, SOLEIL Light Source. The Co edge XAS spectra were recorded in fluorescence mode, whereas, depending on the loading, the Pt edge XAS spectra were measured in transmission and fluorescence mode. A Si(111) double crystal monochromator was used in combination with a Ge 36-element or 5-element detector for the fluorescence measurements, and for the transmission ionization chambers with lengths of 15 and 30 cm were filled with N_2. The averaged XAS spectra were analysed by using the IFEFFIT software package[45]. In principle, the raw spectra were aligned, averaged, background corrected and normalized by the edge step. After conversion of the energy units (eV) into photoelectron wave number k units (Å^{-1}), the resulting $\chi(k)$ functions for XAS spectra were weighted with k^2 and then Fourier transformed to obtain pseudo-radial structure functions. EXAFS spectra of the pure Pt and Co foils as references were used to estimate the amplitude reduction factors (S_0^2).

X-ray total scattering. X-ray total scattering data were obtained at beamline 11-ID-B at the Advanced Photon Source, Argonne National Laboratory. The data were collected from a sample dispersed on Kapton foil, and the signal from the foil was subtracted before further treatment. The data were obtained using an X-ray wavelength of 0.2112 Å, using the rapid-acquisition PDF set-up[46]. PDF analysis was done in PDFgetX3[47] and PDFgui[48]. These show that the Pt networks contain nanocrystalline Pt in the expected fcc structure (Fig. 4a). Owing to the much higher X-ray scattering power of Pt compared to that of Co, as well as the lower amount of Co present in the leached sample, Pt completely dominates the PDF. The refined unit-cell parameter is 3.85 Å, which is much lower than the 3.92 Å reported for bulk Pt. This agrees with the EXAFS results, in which short Pt–Pt

distances were also observed. Considering the fit using the simple fcc Pt structure in Fig. 4a, the model describes the intense peaks in the low *r* region well, whereas the smaller features seen in the PDF from ~18 Å are not described by the model. However, when a fcc structure with a lower refined unit-cell parameter of 3.83 Å is fitted to the range from 18 to 40 Å, the features match well. Further details on the PDF modelling are given in the Supplementary Information.

Data availability

The data supporting the findings of this study are available within this article and its Supplementary Information, or from the corresponding author upon reasonable request. Source data are provided with this paper.

Code availability

The X-ray total scattering analysis and modelling were done in PDFgetX3 and PDFgui. The fitting parameters can be found in the Supplementary Information. The XAS data were analysed by using the IFEFFIT software. DFT calculations were performed with Gpaw and ASE, which are open source codes. The structure and script can be found on the website of the Department of Chemistry, University of Copenhagen.

References

43. Mayrhofer, K. J. J., Ashton, S. J., Kreuzer, J. & Arenz, M. An electrochemical cell configuration incorporating an ion conducting membrane separator between reference and working electrode. *Int. J. Electrochem. Sci.* **4**, 1–8 (2009).
44. Kalliat, M., Kwak, C. & Schmidt, P. in *New approaches in coal chemistry* (eds Blaustein, D., Bockrathand, B. & Friedman, S.) 3–22 (American Chemical Society, 1981).
45. Newville, M. IFEFFIT: interactive XAFS analysis and FEFF fitting. *J. Synchrotron Radiat.* **8**, 322–324 (2001).
46. Chupas, P. J. et al. Rapid-acquisition pair distribution function (RA-PDF) analysis. *J. Appl. Crystallogr.* **36**, 1342–1347 (2003).
47. Juhás, P., Farrow, C. L., Yang, X., Knox, K. R. & Billinge, S. J. L. Complex modeling: a strategy and software program for combining multiple information sources to solve ill posed structure and nanostructure inverse problems. *Acta Crystallogr. A* **71**, 562–568 (2015).
48. Farrow, C. L. et al. PDFfit2 and PDFgui: Computer programs for studying nanostructure in crystals. *J. Phys. Condens. Matter* **19**, 33 (2007).

Acknowledgements

This work was supported by the Danish DFF through grant no. 4184-00332, the Villum Center for the Science of Sustainable Fuels and Chemicals (grant no. 9455) and the Danish National Research Foundation Center for High-Entropy Alloys Catalysis (CHEAC). M.A. acknowledges funding from the Swiss National Science Foundation (SNSF) via project no. 200021_184742. G.W.S. and V.B. acknowledge support from BMBF for funding the validation (VIP+) project 3DnanoMe (FKZ 03VP06451). The authors acknowledge the collaboration with L. T. Kuhn and S. B. Simonsen concerning TEM measurements, A. Mingers for ICP-MS measurements, G. Cibin, S. Belin and M. Nachtegal for technical support at the Quick EXAFS beam line, B18, Diamond Light Source (DLS), the ROCK beam line (proposal ID 20180795) of Synchrotron SOLEIL and the Super XAS beamline, X10DA, of the Swiss light source (SLS) of the Paul Scherrer Institute, respectively. The work at the ROCK beamline was supported by a public grant overseen by the French National Research Agency (ANR) as part of the 'Investissements d'Avenir' programme (reference ANR10-EQPX45). A.D. and M.O. received funding from the DFG (FOR2213, TP9) and the Federal Ministry of Education and Research (BMBF, ECatPEMFC, FKZ 03SF0539). K.M.Ø.J. and M.J. are grateful to the Villum Foundation for financial support through a Villum Young Investigator grant (VKR00015416). We furthermore thank DANSCATT (supported by the Danish Agency for Science and Higher Education) for support. This research used resources at the Advanced Photon Source, a US Department of Energy (DOE) Office of Science User Facility operated for the DOE Office of Science by Argonne National Laboratory under Contract no. DE-AC02-06CH11357.

Author contributions

G.W.S. and M.A. designed and proposed the research direction, analysed the results and drafted and wrote the paper. G.W.S. performed and analysed electrochemical, XAS, SEM, TEM and EDX measurements as well as plasma technical experiments. A.W.J. designed, performed and analysed the electrochemical experiments and co-wrote the paper. J.Q. collected and analysed SAXS, XAS and TEM data and co-wrote the paper. A.Z. helped acquire, analyse and interpret ex situ and in situ XAS measurements and electrochemical measurements. F.B. performed electrochemical measurements and XAS data. M.O. collected and analysed XAS data and co-wrote the paper. A.D. acquired and analysed XAS data. J.J.K.K. acquired and analysed SAXS data. T.E.L.S. and S.K. acquired and analysed STEM tomography. M.J. and K.M.Ø.J. acquired, analysed and interpreted the PDF data. K.A. and V.B. contributed to the planning, execution and interpretation of plasma technical experiments. H.W. and J.R. executed the DFT calculations, interpretation of the data and co-wrote the paper. J.S. and K. Č. acquired and analysed the HAADF STEM elemental distribution and co-wrote the paper. M.E.-E. interpreted the electrochemical data and co-wrote the paper. A.Q. acquired, analysed and interpreted the XPS experiments. All the authors discussed the results and participated in writing the manuscript.

Competing interests

The authors declare no competing interests.

Additional information

Supplementary information is available for this paper at https://doi.org/10.1038/s41563-020-0775-8.

Correspondence and requests for materials should be addressed to G.W.S. or M.A.

Reprints and permissions information is available at www.nature.com/reprints.